PNAS
www.pnas.org

Supplementary Information for

A stepwise mechanism for aqueous two-phase system formation in concentrated antibody solutions

Bradley A. Rogers,[a] Kelvin B. Rembert,[a] Matthew F. Poyton,[a] Halil I. Okur,[a] Amanda R. Kale,[a] Tinglu Yang,[a] Jifeng Zhang,[c,1] Paul S. Cremer[a,b,1]

[a]*Department of Chemistry and* [b]*Department of Biochemistry and Molecular Biology, The Pennsylvania State University, University Park, Pennsylvania 16802*
[c]*Drug Delivery and Device Development, Medimmune, One Medimmune Way, Gaithersburg, Maryland 20878*

[1]Corresponding authors: Jifeng.Zhang@sanofi.com (J.Z.); psc11@psu.edu (P.S.C.)
The current address for J.Z. is Sanofi, Biologics Drug Product Development, One Mountain Road, Framingham, MA 01701, USA

This SI file includes:

Other supplementary materials for this manuscript include the following:

Supporting Information Text

1. Materials and Methods

Sample Preparation. An IgG1 mAb with a pI of 8.2 was produced, purified and formulated at 116 mg/mL in 10 mM sodium acetate at pH 4.8. Samples were diluted from this stock solution. NaCl (EMD Millipore), Na_2HPO_4 and NaH_2PO_4 (Sigma Aldrich) were at least 99% pure. PEG-3350 was purchased from Spectrum Chemical. All salts as well as PEG were used as received. 18.2 MΩ·cm purified water from a Barnstead Nanopure water purification system (Thermo Scientific) was used to prepare solutions. Concentrated stock solutions were mixed volumetrically to achieve the desired concentrations. The samples were then incubated in a water bath at 318 K for 30 minutes along with periodic mixing to ensure homogeneity. To make temperature gradient measurements, the solutions were loaded into 12 mm x 1 mm x 0.1 mm rectangular borosilicate glass capillary tubes (VitroCom, Inc.), by capillary action, and sealed with wax to avoid sample evaporation and convection.

Liquid formulations of therapeutic mAbs are typically prepared under conditions where the protein bears a net positive charge. As such, phosphate buffer was employed to achieve a pH of 6.8, which was below the pI. We note, however, that histidine and acetate buffers are more commonly employed in mAb formulations. NaCl was added to screen long-range electrostatic repulsions between the net positively charged mAbs. The PEG-3350 concentration was adjusted to induce phase separation at temperatures between 278 and 308 K.

Controlling the pH of mAb Solutions. We found the final pH of mixed solutions to be dependent on the mAb concentration, due to the protein's buffer capacity. As such, 0.5 M phosphate buffer stock solutions were employed to maintain pH 6.8 ± 0.1 for all mAb concentrations. Our approach was to mix 2 sodium phosphate solutions, a 0.5 M NaH_2PO_4 solution and a 0.5 M Na_2HPO_4 solution, at various ratios to generate a series of buffer stock solutions and choose the ratio that matched the desired final pH upon mixing with the other solution components. In this method, appropriate amounts of H_3O^+ and OH^- were added to the sample to achieve the desired pH, while maintaining constant phosphate and chloride concentrations. This avoided tedious small volume additions of a strong acid (HCl) or base (NaOH). It should be noted that the total Na^+ ion concentration changed by less than ~ 7 mM between the 20 and 100 mg/mL mAb. In other words, the pH and ionic strength were held essentially constant for all of the solutions.

Calibrating the Temperature Gradient. For each experiment, the temperature gradient was calibrated by placing 2 reference solutions alongside the mAb samples of interest. Both of the reference solutions contained 10 mg/mL poly(*N*-isopropyl acrylamide) (PNIPAM) and a given NaCl concentration in H_2O. The PNIPAM was purchased from Polymer Source and had a MW = 1.868×10^5 g/mol. The lower critical solution temperature (LCST) of each reference solution was obtained with a melting point apparatus that measured light scattering intensity as the temperature was increased at a rate of 0.5 K/min. Specifically, the LCST was determined at the onset of scattering intensity relative to the flat, low intensity baseline observed at lower temperatures. When placed onto the temperature gradient device, the reference solutions became cloudy at temperatures above the LCST. The pixel position of the LCST was obtained by the onset of light scattering intensity relative to the low intensity baseline on the cold side of the capillary. The temperature gradient was calculated using the pixel positions and the LCST values of the 2 samples, assuming a linear relationship between position and temperature (1). We note that the temperature gradient was imposed on a 6 mm portion of the 12 mm glass capillary tube. This is half of the distance employed for the temperature gradient in previous studies (1), which displayed a linear temperature dependence. We confirmed the linearity of the temperature gradient device used in this work by calibrating the instrument as described above and then measuring the LCST of PNIPAM in 0.8 M NaCl. The value determined on the temperature gradient was similar to the value determined with a melting point apparatus.

2. Side-On Imaging of ATPS Formation and the Thermodynamics of the Colloidal Phase Diagram

Imaging ATPS Formation on a Temperature Gradient Device versus under Isothermal Conditions. In a control experiment, the 90 mg/mL mAb solution with 20 mg/mL PEG-3350, 15.5 mM NaCl, and 22.7 mM phosphate buffer at pH 6.8 was introduced onto the gradient at a constant temperature of 318 K, which is above T_{ph} (Fig. S1*A*). The image appeared dark across the entire sample, confirming that the homogeneous solution did not scatter very much light. In comparison, there was significant light scattering from the droplets that formed below T_{ph}, at t = 1 min, after being introduced onto a linear temperature gradient of 278 to 318 K (Fig. S1*B*). As can be seen at 4 and 7 min, ATPS formation above T_{gel} resulted in a reduction of light scattering intensity (Fig. S1*C-D*). Eventually, the ATPS formation yielded a completed ATPS above T_{gel}, e.g. 60 min (Fig. S1*E*).

Throughout the manuscript, the reduction in light scattering intensity with time was attributed to the growth of droplets and the formation of a clear ATPS within the sample capillary. To confirm this interpretation, we acquired side-on images of macroscopic phase separation in a 1.5 mL microcentrifuge tube at constant temperature. These constant temperature experiments were also performed on a 90 mg/mL mAb solution with 20 mg/mL PEG-3350, 15.5 mM NaCl, 22.7 mM phosphate buffer at pH 6.8. The sample was incubated and periodically mixed for 30 min at 318 K (Fig S1*F*). To initiate a temperature quench, the sample was removed from the water bath (318 K) and placed at room temperature (293 K) or in a cold room (277 K). The images for the 293 K and 277 K quench experiments are shown in the upper and lower images of Fig S1*F-I*, respectively. The images were obtained over time to follow the macroscopic phase separation at 1, 15, and 60 minutes in Fig. S1*G*, S1*H*, and S1*I*, respectively. As expected, the 293 K quench resulted in the formation of a clear ATPS after 60 minutes, while the deeper quench at 277 K formed a gel that did not macroscopically phase separate, even after several weeks.

Measuring Transition Temperatures on the Temperature Gradient. The 3 transition temperatures were obtained quantitatively from line scans of scattering intensity as a function of temperature. The phase separation temperature, T_{ph}, was determined just after the temperature gradient stabilized, t = 1 min. The value of T_{ph} was defined as the onset of intensity, relative to the region of low and flat scattering intensity at high temperature, as shown by the intersection of the 2 red tangent lines in Fig. S2*A*. The metastable transition temperature, T_{meta}, was determined at the first time point where ATPS formation came to completion below T_{ph}. This time point occurred when the light scattering reached a minimum in intensity and did not change as more time past. In most cases, the time point for the metastable transition determination was around t = 7 min. The metastable transition temperature was determined by the onset of light scattering intensity, relative to the nearly completed ATPS at lower temperatures, as shown by the intersection of the 2 tangents shown with green lines in Fig. S2*B*. Finally, the gelation temperature, T_{gel}, was determined from the line scan at t = 60 min, where ATPS formation had been completed or became kinetically trapped at all temperatures below T_{ph}. Specifically, the gelation transition temperature was determined by the onset of light scattering, relative to the completed ATPS baseline, as shown by the intersection of the 2 solid blue tangent lines in Fig. S2*C*. We note that the 4 line scans provided in the main text, Fig. 2, have been normalized to the highest and lowest intensities observed in temperature and time during the experiment. Specifically, the data for all 4 line scans were normalized by subtracting the lowest intensity data point and then dividing the line scan data by the difference between the highest and lowest intensity data points. As such, the normalized line scans have values that ranging from 1 to 0.

Constructing a Colloidal Phase Diagram in the Presence of PEG. We measured the 3 transition temperatures as a function of mAb concentration at 20 mg/mL PEG-3350 to construct the phase diagram shown in Fig. S3. As can be seen, T_{ph} increased sharply at low concentration, but began leveling-out by 100 mg/mL (red points in Fig. S3). Below the binodal curve, we observed a metastable region that was bound by T_{meta} at low temperature (green data points in Fig. S3) for solutions containing more than 50 mg/mL mAb. T_{meta} increased with mAb concentration in a similar fashion to the binodal curve up to 100 mg/mL

mAb and defined the spinodal curve (green curve in Fig. S3). The spinodal should meet the binodal at the critical point, as shown schematically in Fig. 1. This intersection was not observed in the employed concentration range, which may indicate that the critical concentration, C_{crit}, was located at higher mAb concentration. The presence of PEG, however, makes the system ternary, consisting of water, protein, and PEG. The ternary nature of the system could cause the phase diagram to have an asymmetric shape or move the critical point away from the binodal maximum (2–5). At lower concentrations, T_{meta} was not measurable due to gelation. Indeed, T_{meta} should be below T_{gel} for mAb concentrations between 20 and 50 mg/mL. We measured T_{gel} at all mAb concentrations to chart the gelation line, below which separation became arrested (blue curve in Fig. S3). For all samples, gelation occurred at or below T_{ph} and T_{gel} increased only slightly with mAb concentration, with a linear slope of 0.05 K*(mg/mL)$^{-1}$. These results suggest that the kinetic barrier associated with arrested ATPS formation is relatively independent of mAb concentration.

3. Kinetic Analysis of ATPS Formation

3-Dimensional Plots of the Light Scattering Data Obtained from the Temperature Gradient Experiments. To visualize the data obtained on the temperature gradient device, we constructed plots of light scattering intensity as a function of both temperature and time for various mAb concentrations. These 3-dimensional plots are provided for 90, 60, 40, and 20 mg/mL mAb conditions in Fig. S4.

Establishing a Stable Temperature Gradient. The time required to establish a steady-state linear temperature gradient across the sample capillary was estimated using 2 independent methods. First, we monitored the apparent position for the lower critical solution temperature (LCST) of PNIPAM as a function of time. A 10 mg/mL PNIPAM sample in 0.8 M NaCl was loaded into a capillary tube and then incubated at 4 °C, where the polymer was soluble. The sample was then introduced onto a pre-equilibrated temperature gradient (278 – 318 K) and line scans of the light scattering intensity were measured across the capillary as a function of time (Fig. S5*A*). At each time point, the line scans showed weak light scattering at lower pixel numbers (cold temperatures) and an onset of light scattering at the LCST located at higher pixel numbers (hot temperatures). The spatial position of the LCST shifted to a higher pixel position as time progressed and the sample capillary established a steady-state temperature gradient.

The apparent LCST pixel position is plotted as a function of time in Fig. S5*B* (blue data points). A schematic illustration of the PNIPAM experiment is provided in Fig. S5*C*. In a separate experiment, a thermocouple was used to acquire direct measurements of the external temperature of a capillary filled with DI water. The thermocouple was fastened to the capillary with a piece of scotch tape as shown in Fig. S5*D*. After introduction of the sample onto the temperature gradient, the temperature read out of the thermocouple was recorded at 1 second intervals. The temperature measured by the thermocouple (red data points) is plotted as a function of time in Fig. S5*B*. These 2 measurements provide an estimate of about 1 minute for the temperature equilibration of samples on the temperature gradient device.

Processing the Time-Dependent Light Scattering Data. The isothermal light scattering decays, i.e. intensity versus time at a specific temperature along the temperature gradient, were processed by a standardized procedure prior to kinetic modeling. Here we provide a sequential demonstration of this procedure for an isotherm measured at 293.3 K for the 90 mg/mL mAb sample with 20 mg/mL PEG-3350. The light scattering intensity, I, was plotted as a function of time, t, after placing the sample onto the temperature gradient (Fig. S5*E*). The solid red vertical line denotes the equilibration time t = 1 min that was required to establish a steady-state heat flow and a stable, linear temperature gradient. The data within this equilibration time window, i.e. t < 1 min, was discarded. Next, the remaining intensity data points were plotted as a function of shifted time, $t_{shifted}$, as shown in Fig. S5*F*. The shifted time accounts for the discarded data by subtracting a temporal shift of 1 minute along the time axis, as shown in Eq. S1. In the last step of data processing, the shifted time intensity data were background corrected by subtracting the residual scattering intensity, I_{back}, and normalized by division by the maximum intensity, I_{max}, as shown in Eq. S2.

The fully processed data (Fig. S5*G*), which was used in the fitting analyses, begins at a normalized intensity, I_{norm}, of 1 at and decays to 0.

$$t_{shifted} = t - 1\ min \quad \text{Eq. S1}$$

$$I_{norm} = \frac{(I - I_{back})}{(I_{max} - I_{back})} \quad \text{Eq. S2}$$

Mechanisms and Kinetic Models of ATPS Formation. The process by which a thermodynamically unstable dispersion (i.e. droplets of densely packed mAbs) could proceed toward an equilibrated ATPS generally should follow 1 of 2 possible mechanisms: coalescence or Ostwald ripening. For coalescence, there are 2 extreme cases. First, in a very dilute suspension of droplets, the collision rate between the droplets can be the rate-limiting step. In this situation, coalescence should resemble a second-order process. At higher concentrations of the droplets, however, the rupture of the interfacial water film between 2 droplets is the rate-limiting step. Under these circumstances, which are valid at the concentrations employed in the present experiments, the kinetics of droplet coalescence become first-order and follow a first-order reaction equation, Eq. S3 (6, 7):

$$N = N_0 exp(-kt) \quad \text{Eq. S3}$$

where the droplet number, N, decays from an initial number, N_o, as a function of time, t, with a first-order rate constant, k.

By contrast, Ostwald ripening is the growth of large droplets at the expense of smaller ones. The origins of this mechanism are understood by changes in solubility, $C(r)$, of a solute with the curvature of the droplet/solution interface or droplet radius, r. Specifically, there is a surface effect that decreases protein solubility with increasing particle radius, r, as can be shown through the Gibbs-Thompson equation, Eq. S4 (8–10).

$$r = C_\infty exp\left(\frac{2\gamma V_m}{rRT}\right) \approx C_\infty \left(1 + \frac{2\gamma V_m}{rRT}\right) \quad \text{Eq. S4}$$

Here, C_∞ is the protein solubility in the protein-poor phase of the completed ATPS, γ is the surface tension of the droplet/water interface, V_m is the molar volume of the protein in the protein-rich phase, r is the radius of a droplet, R is the ideal gas constant, and T is the absolute temperature. A decreasing concentration gradient in the radial direction extends out from the surface of sufficiently small droplets, while an increasing gradient exists near larger droplets (11). Such gradients ultimately lead to diffusive transfer of material from small droplets to larger ones. Throughout this process, the average droplet radius increases with time as sufficiently large ones release fewer and fewer proteins per unit surface area into the bulk. The droplet number, N, in a system undergoing Ostwald ripening should follow second-order kinetics described by Eq. S5 (10, 12).

$$\frac{1}{N} - \frac{1}{N_0} = kt \quad \text{Eq. S5}$$

The idea that droplets grow via an Ostwald-like ripening process has been proposed for cluster growth in a variety of protein systems (13–15).

Fits to the KWW Model. The scattering decays were best fit to the Kohlrausch-Williams-Watts, KWW,

model described by Eq. 1. The normalized light scattering data and KWW fits for each isotherm are provided in Fig. S6. The data are organized into 3 panels corresponding to the 90, 60, and 40 mg/mL mAb samples. The KWW fits provided an apparent rate constant for ATPS formation, k. The exponent β accounts for cooperative ($\beta > 1$) and anti-cooperative ($\beta < 1$) features of the decays observed at high and low temperatures, respectively.

Time Scale of the Temperature Gradient Measurements. For the experiments presented in this work, the sample-containing capillary is placed in contact with the hot and cold sides of the device at $t = 0$ s. As protein-rich droplets form, we expect the light scattering to increase. However, a time period of ~60 s is required to form a steady-state temperature gradient across the sample. As such, the kinetic analysis was only performed on data collected after 60 s, after which the intensity decreases monotonically. This slow time scale (~10^1-10^3 s) should be too slow to report on nucleation events (~10^{-2}-10^0 s) (16). As such, we expect that changes in scattering intensity report on droplet growth and coalescence, which is discussed in more detail below.

Scattering Intensity Reports on Both Droplet Size and Concentration. The scattering intensity measured on an optical dark-field microscope depends on both the concentration and size of the droplets inside of the sample-containing capillary. At early times after a sample has been cooled below T_{ph}, droplets should nucleate until a steady-state number of droplets have formed. We expect that by 60 s, the changes in the light scattering intensity should report on the growth rate of a steady-state concentration of droplets and their coalescence into an ATPS.

The effect of droplet size on the light scattering intensity depends on the ratio of the droplet radius, r, relative to the wavelength of the incident light, λ ~ 350-720 nm. Scattering from small droplets with $r <$ ~25 nm should be weak and governed by Raleigh scattering, which dominated when the value of r/λ is less than 5. The light scattering from large droplets with a $r >$ ~ 2.5 μm should also be weak and governed by the geometric scattering, which is relevant for values of r/λ that are greater than 5. Based on these arguments, the homogeneous state, consisting mostly of protein monomers with r ~ 5 nm, and the equilibrated ATPS with r ~ 5 μm should both be nearly optically transparent. Thus, the intensity in TGM experiments should be dominated by Mie scattering, which dominates for values of r/λ ~ 0.5. These arguments suggest that droplets ranging from r ~ 25 nm to 2.5 μm produce the signal observed in the TGM kinetics data. Indeed, nucleation events, which involve monomer, dimers, trimer, and higher order oligomers are small and should not scatter much light.

Additional Considerations for the Kinetic Analysis. Our mechanistic interpretations are simplified and rely on the assumption that the scattering intensity reports on the number of droplets, N. In reality, however, the intensity depends on both the concentration and size of protein-rich droplets, as discussed above. We note that additional complications could arise from non-spherical droplet geometry (e.g. networks formed in the gel state), variations in ensemble size distributions, multiple scattering, the collection of light over integrated scattering angles, and the use of a continuum light source.

Estimates for Diffusion Along the Temperature Gradient. Another important point of concern is the diffusion of material (e.g. proteins or droplets) along the sample capillary during an experiment. The diffusion coefficient of particle, D_{SE}, can be approximated by the Stokes-Einstein equation, provided in Eq. S6,

$$D_{SE} = \frac{k_B T}{6\pi\eta r} \qquad \text{Eq. S6}$$

where k_B is the Boltzmann constant, T is the temperature, η is the viscosity, and r is the radius of the particle.

The value of D_{SE} at 295 K for a mAb monomer is ~5x10^{-7} cm^2/s, assuming r = 5 nm and the viscosity is that of pure water, 8.9x10^{-4} Pa*s. Under the same solution conditions, a droplet with r = 1 μm is expected to diffuse at a slower rate, D_{SE} = 2.4*10^{-9} cm^2/s. The mean displacement, $\langle \Delta^2 x \rangle^{1/2}$, of these particles at various time points during the experiment can be estimated using Eq. S7.

$$\langle \Delta^2 x \rangle^{1/2} = (6 D_{SE} t)^{1/2} \qquad \text{Eq. S7}$$

The values of $\langle \Delta^2 x \rangle^{1/2}$ for the monomer at 1, 15, and 60 min were 0.132, 0.512, and 1.024 mm. The values of $\langle \Delta^2 x \rangle^{1/2}$ for the droplet at 1, 15, and 60 min were 0.009, 0.036, and 0.072 mm. Displacement along the temperature gradient has also been considered by multiplying the mean displacement by the temperature gradient (6.66 K/mm). The temperature displacement for the monomer at 1, 15, and 60 min were 0.881, 3.414, and 6.827 K. The temperature displacements for the droplet at 1, 15, and 60 min were 0.062, 0.241, and 0.483 K. As can be seen, the mAb monomer shows considerable diffusion during the experiment, while the droplets are more localized. Since droplets form within 1 minute and ATPS formation is completed in about 15 minutes, only the lower end of these ranges need to be considered. Indeed, a growing droplet would probably experience less than a quarter of a degree temperature change before ATPS is completed.

Further Discussion of the Proposed 2-Step Mechanism. The simplified reaction scheme proposed in Eq. 3 is complicated by the fact that ATPS formation should resemble the reaction scheme proposed in Fig. 7*A*. Indeed, droplet growth should involve a large number of sequential associations, rather than a single pre-equilibrium step. Droplets might contain a numbers of proteins, n, ranging from a few to many millions. If we assume that the rate constant of monomer association, k_n, is diffusion-limited, then it should not depend on the size of the droplet. On the other hand, the rate constant of monomer dissociation, k_{-n}, should vary with droplet size due to surface curvature effects. We expect the value of k_{-n} to be enhanced for oligomers and small droplets, where the droplet surface is more curved and less protein-protein interactions have to be broken to dissociate a monomer into the bulk solution. For large droplets, however, we expect k_{-n} to approach a limiting value as the local curvature of the droplet surface becomes flat. The values of k_n and k_{-n} are expected to be size-independent for the larger droplets that are relevant for the temperature gradient measurements. As such, we advocate the use of single parameters to describe the rate constants of the forward, k_1, and reverse steps, k_{-1}, of late-stage growth.

A more detailed reaction equation for ATPS formation and a conversion of intensity to droplet number or size would be necessary to quantitatively account for these complications. Nevertheless, the simplified model provided in Eq. 3 offers a qualitative explanation for the effects of temperature on the apparent rate constant of ATPS formation determined from the fits to the KWW model.

Temperature Dependence of the KWW Parameters. The cooperativity exponents, β, and apparent rate constants, k, determined for the 90, 60, and 40 mg/mL mAb solutions with 20 mg/mL PEG-3350 are plotted as a function of temperature in Fig. S7*A* and S7*B*, respectively. Moreover, Arrhenius plots constructed from the measurements of k are provided in Fig. S7*C*. We observed several generic features of the kinetics data for all mAb concentrations: k became moderately slower near T_{ph}, k was enhanced at intermediate temperatures, and k became arrested near T_{gel}.

Interestingly, k slows down near T_{ph} most dramatically under the 90 mg/mL conditions (red data in Fig. S7*B*). The hindrance of ATPS formation at the highest temperature is consistent with an accelerated rate of dissociation. Indeed, T_{ph} occurs at a lower temperature for the 60 and 40 mg/mL mAb conditions, which prohibits measurements of ATPS formation at higher temperature where dissociation would be accelerated further. The attenuation of k near T_{ph}, is mirrored by an increase in β. For the 90 mg/mL sample, the nearly constant value of $\beta \sim 1.5$ at intermediate temperatures (293 - 299 K) increased slightly near T_{ph} ($T > 299$ K). The more pronounced cooperativity in ATPS formation may indicate a prolonged lifetime of droplets

due to enhanced dissociation. The rate of ATPS formation was faster at higher mAb concentrations for all temperatures that did not gel (blue to green to red data in Fig. S7*B* above $T \sim 292$ K). At lower mAb concentrations, the time required for droplet growth should be longer, thereby prolonging ATPS formation.

The natural log of the time constant for ATPS formation, $\ln(\tau)$, obtained from the negative of $\ln(k)$, represents a characteristic time scale for processes that contribute to ATPS formation. These time constants were found to lengthen dramatically as the temperature was lowered into the gel state for all mAb concentrations. The time constants are plotted on a natural log scale for the 3 protein concentrations in Fig. S7*D*. It should be noted that the range of temperatures used in the VFT analysis were characterized by $\beta < 1$. The fitted parameters of gelation determined from fitting to the VFT model are provided in Table S1. It would be informative to compare the fragility index (D) of the gels formed in mAb solutions to other soft colloidal systems. However, measurements of the fragility index for colloids are commonly based on concentration-dependent particle dynamics, rather than the temperature dependence of ATPS formation kinetics employed in this work (17, 18). It should be note that the values of β for the 40 mg/mL sample lack a region of intermediate temperatures where β is constant. This provides an additional indication that gelation occurs in the metastable region of the phase diagram at lower mAb concentrations.

The apparent activation energies for ATPS formation, $E_{A,app}$, were obtained from the Arrhenius plots in Fig. S7*C*. We calculated the values for $E_{A,app}$ by multiplying the first derivative of the Arrhenius plot by the negative of the ideal gas constant. The results are plotted as a function of temperature in Fig. S8. As can be seen in Fig. S8*A*, $E_{A,app}$ shows similar temperature dependence for all 3 mAb concentrations. At temperatures below 293 K, ATPS formation is hindered by a large positive $E_{A,app}$ due to gelation. On the other hand, at intermediate temperatures, $E_{A,app}$ shows an average close to 1 kcal mol^{-1}. With increasing temperature, $E_{A,app}$ clearly becomes negative with an average of ~ -35 kcal mol^{-1}. For clarity, the data are also plotted separately for each mAb concentration in Fig. S8*B* - S8*D*. For each concentration, the average and standard deviation of the $E_{A,app}$ values are provided for the spinodal (green text) and metastable (red text) regions.

Connection between the Thermodynamics and Kinetics of Phase Separation in the Metastable Region. We expect droplet growth to dominate the kinetics of ATPS formation in the metastable region, where we measured a negative $E_{A,app}$. Below, we consider 2 possibilities for the observed negative $E_{A,app}$.

Case 1 is that the free energy of the thermodynamic states in Fig. 7*B* change with temperature. Classical nucleation theory predicts that the kinetics in the metastable region are controlled by Case 1 (19). In particular, the theory predicts that the steady-state growth rate increases linearly with supersaturation, while the rate of nucleation should increase exponentially (19–22). We estimated the supersaturation at each temperature from the phase diagram to test the validity of Case 1 and also to test the idea that the apparent rate constants of ATPS formation, k, report on droplet growth, rather than nucleation. Supersaturation, s, was estimated using Eq. S8,

$$s = ln\left(\frac{C_o}{C_{poor}}\right) \qquad \text{Eq. S8}$$

where C_o is the initial protein concentration, and C_{poor} is the equilibrium concentration of the protein-poor phase after a temperature quench. We obtained the values for C_{poor} at each temperature by fitting the binodal phase diagram (T_{ph} vs C) to Eq. S9, where T_{crit} and C_{crit} are the critical temperature and concentration, while A and β are empirical parameters that determine the shape of the phase boundary (23–26). It should be emphasized that T_{crit} and C_{crit} are nominal values as the measurements were only made up to 100 mg/mL and Eq. S9 assumes that the binodal curve is symmetric despite the ternary nature of the system, which has been shown to influence the shape of colloidal phase diagrams (2–5, 23, 25). Nevertheless, the data below

100 mg/mL was well-modeled by Eq. S9.

$$T_{ph} = T_{crit}\left[1 - A\left(\frac{C_{crit} - C}{C_{crit}}\right)^{1/\beta}\right] \qquad \text{Eq. S9}$$

This analysis for estimating the supersaturation is depicted schematically in Fig. S9. Remarkably, the dependence of k on s, provided in Fig. S9*B*, is approximately linear in the metastable region (black line over the red data points in Fig. S9*B*), until reaching a maximum value at T_{meta}. At even higher values of s (lower temperature) the rate constant became arrested due to gelation (blue data points). As described in the main text, this analysis suggests that the negative value of $E_{A,app}$ is related to the enhanced thermodynamic driving force for demixing as the temperature of the solution is decreased below T_{ph}.

In other words, the value of $E_{A,app}$ is related to the change in free energy with respect to temperature. Supersaturation should be related to the change in free energy upon forming protein-protein interactions (e.g. adding a protein to a droplet). The concept of supersaturation is included in Fig. 7 by the difference in free energy between the initial state (monomer and droplet) and the intermediate state (droplet). Based on Fig. S9, the change in free energy should be larger at lower temperatures. As a consequence, we expect the activation energy required for dissociation to increase and droplet growth to accelerate.

One could imagine a second case involving thermodynamic states that are fixed. Under Case 2, the reaction coordinate is again a multi-step process involving a reversible first step and an irreversible second step. The negative $E_{A,app}$ would imply that the reverse reaction in the first step has a large activation energy. As the temperature is lowered, the rate of the reverse reaction decreases sharply and the reversibility of the first step (i.e. droplet growth) is impeded, leading to an accumulation of intermediate droplets. As such, the observed rate of ATPS formation increases with cooling, until eventually it becomes limited by the second step of droplet coalescence in the spinodal region.

The negative $E_{A,app}$ in the metastable region (black line over the red data in Fig. 4*B*) would support the idea that LLPS is limited by a pre-equilibrium step in a multistep reaction (Fig. 7) (27). In fact, when k is collectively influenced by k_1, k_{-1}, and k_2, there should be 3 activation energies to take into account: 2 corresponding to the reversible steps of the pre-equilibrium ($E_{A,1}$ and $E_{A,-1}$ in Fig. 7*B*) and 1 for droplet coalescence in the forward direction ($E_{A,2}$ in Fig. 7*B*). The relative magnitudes of the forward and reverse activation energies determine whether the overall apparent activation energy is positive or negative ($E_{A,app} = E_{A,1} + E_{A,2} - E_{A,-1}$). To estimate the value of $E_{A,-1}$ for the Case 2 scenario, we assumed that the association reaction was essentially diffusion-limited. Under diffusion-limited conditions, k_1 should exhibit a weak temperature dependence, proportional to the diffusion coefficient (28, 29). Based on the small barrier for coalescence ($E_{A,2}$ = 1 kcal mol^{-1}) measured in the spinodal region and the assumption of diffusion-limited association ($E_{A,1} \sim 0$ kcal mol^{-1}), the apparent activation energy measured in the metastable region provides an approximate barrier for the dissociation of protein monomers from protein-rich droplets ($E_{A,-1} \sim 35$ kcal mol^{-1}). This is in agreement with the apparent activation energy for dissociating protein-protein complexes by electrospray mass spectrometry (30).

Although Case 2 might appear to offer a plausible interpretation for the negative $E_{A,app}$ in the metastable region, the supersaturation analysis presented in Fig. S9 suggests the thermodynamic states do change with temperature. Thus, the temperature-dependent kinetics of ATPS formation are more accurately described by Case 1.

Figures

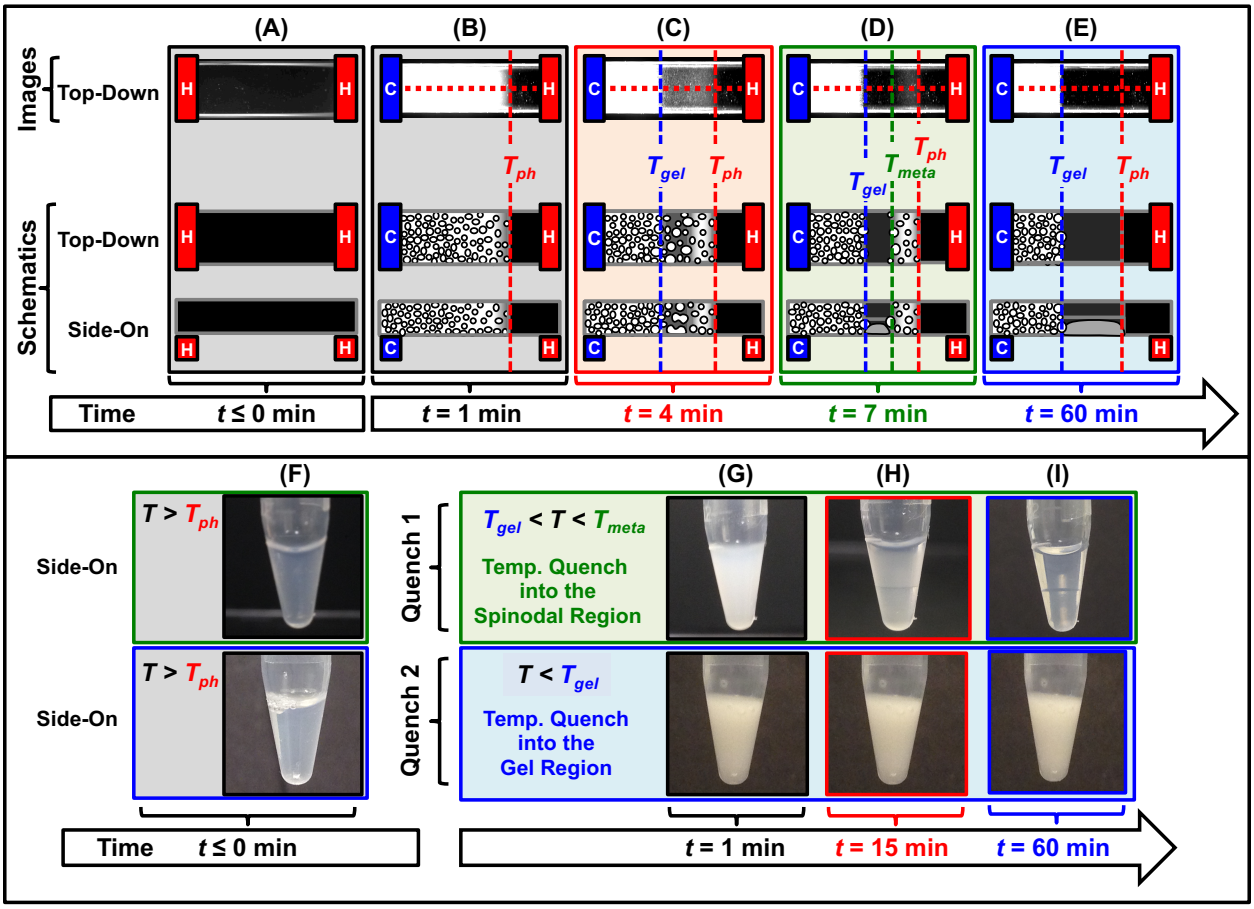

Figure S1. Dark-field images and schematics of phase separation on the temperature gradient device versus images of temperature quenches performed on macroscopic samples. The dark-field images of the temperature gradient experiments are provided at 5 time points (columns *A*-*E*) during the separation of a solution containing 90 mg/mL mAb and 20 mg/mL PEG-3350. Specifically, we show (*A*) an image of a sample exposed to a constant temperature (318 K) versus a linear temperature gradient (278 – 318 K) at (*B*) 1 min, (*C*) 4 min, (*D*) 7 min, and (*E*) 60 min after sample introduction. The white circles in the schematics represent protein-rich droplets, which scatter light (*B*-*E*). The droplets coalesce to form the clear protein-rich phase of an ATPS, as depicted by the large grey droplet (*D*-*E*). For comparison, we also recorded images of the phase separation process in centrifuge tubes upon temperature quenches at (Quench 1) 293 K and (Quench 2) 277 K, which reside in the spinodal and gel regions, respectively. We provide (*F*) an image recorded at 318 K, prior to the temperature quench, versus images captured at (*G*) 1 min, (*H*) 15 min, (*I*) 60 min after the temperature quench.

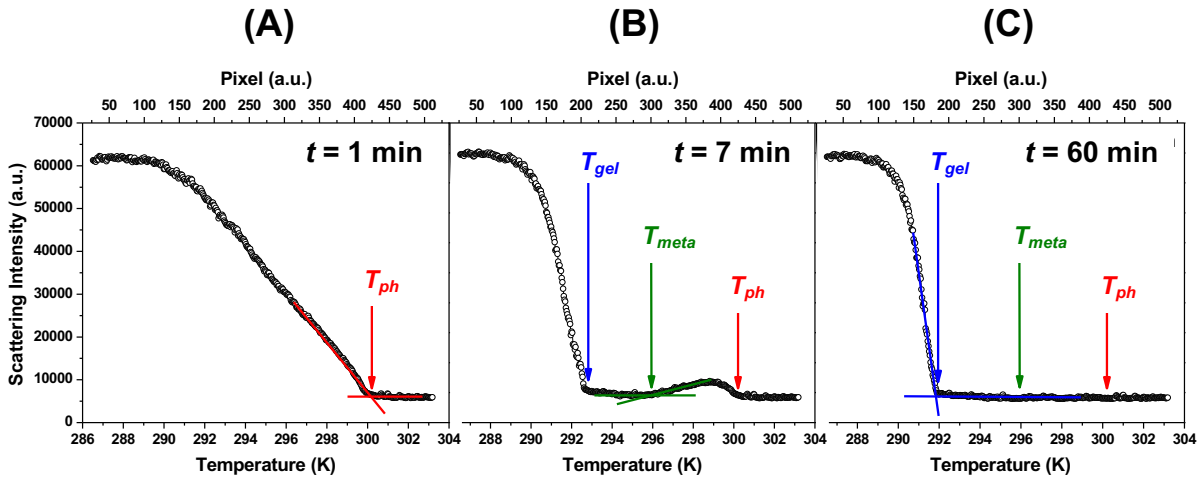

Figure S2. Line scans of scattering intensity as a function of temperature at 3 time points of phase separation for the 90 mg/mL mAb and 20 mg/mL PEG-3350 solution. The line scans were obtained from the dark field images shown in Fig. S1. The line scans are given for (*A*) t = 1 min, (*B*) t = 7 min, and (*C*) t = 60 min. The solid lines are provided as visual aids for the transition temperature determinations of T_{ph} (red lines), T_{meta} (green lines), and T_{gel} (blue lines).

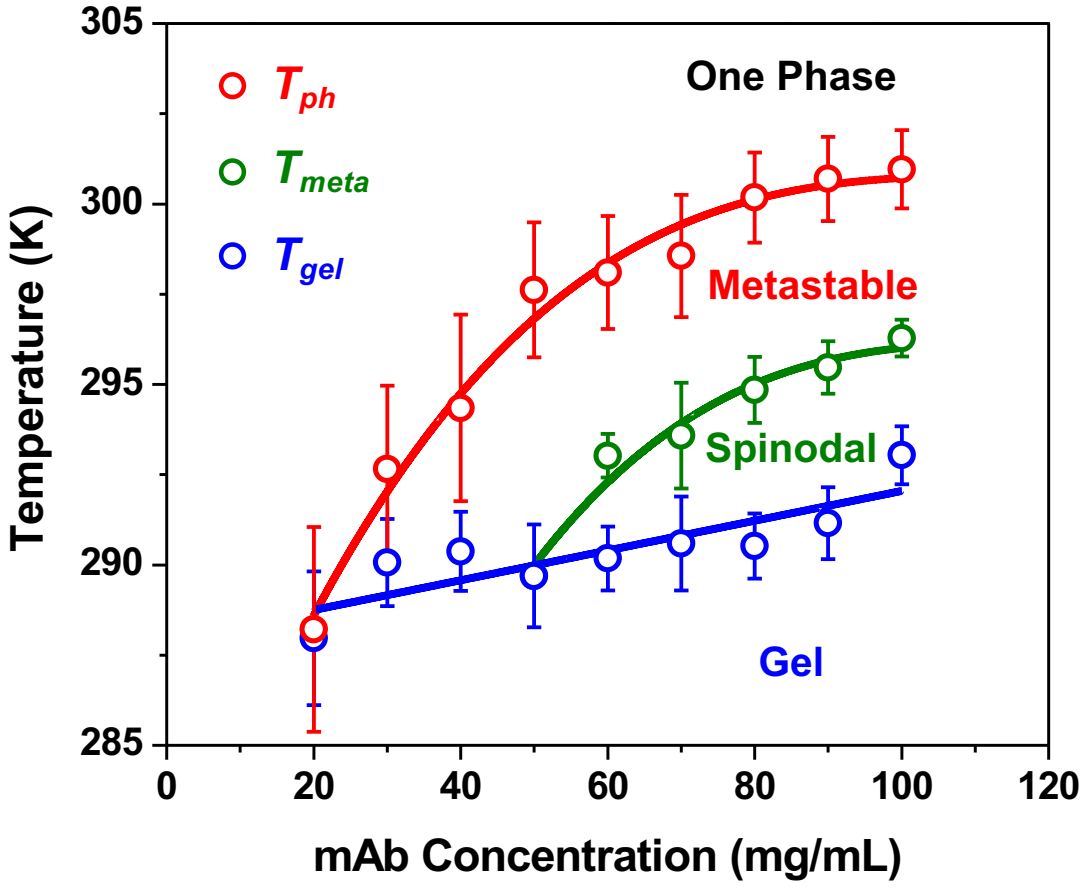

Figure S3. Colloidal phase diagram measured at 20 mg/mL PEG-3350. T_{ph} (red data points) and T_{gel} (blue data points) were measured at t = 1 min and t = 60 min, respectively; while T_{meta} (green data points) was measured at the first time point when ATPS formation had come to completion below T_{ph}. The red and green curves are guides to the eye, while the blue curve is a linear fit to the T_{gel} data.

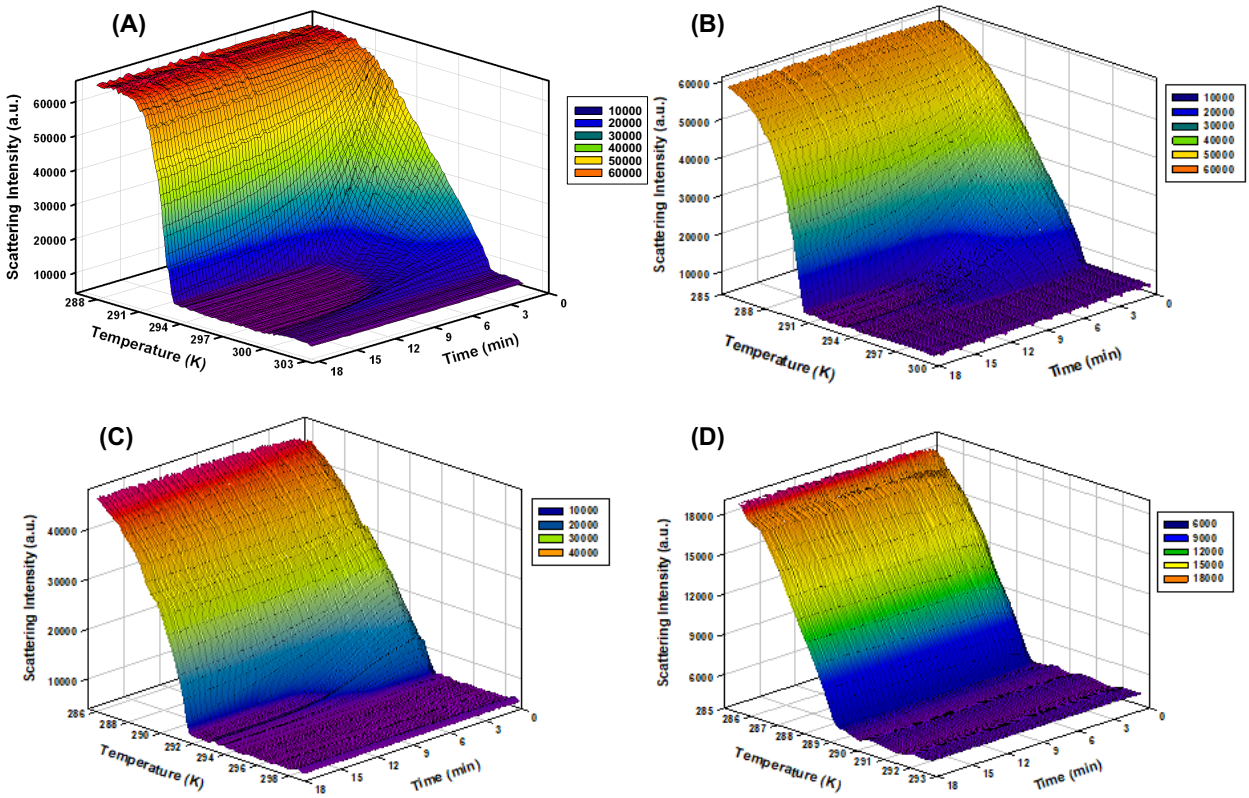

Figure S4. 3-dimensional plots of light scattering intensity as a function of both temperature and time for (*A*) 90 mg/mL, (*B*) 60 mg/mL, (*C*) 40 mg/mL, and (*D*) 20 mg/mL mAb, all containing 20 mg/mL PEG-3350. The plots are shown at a temporal resolution of 15 seconds for (*A*) and 5 seconds for (*B-D*).

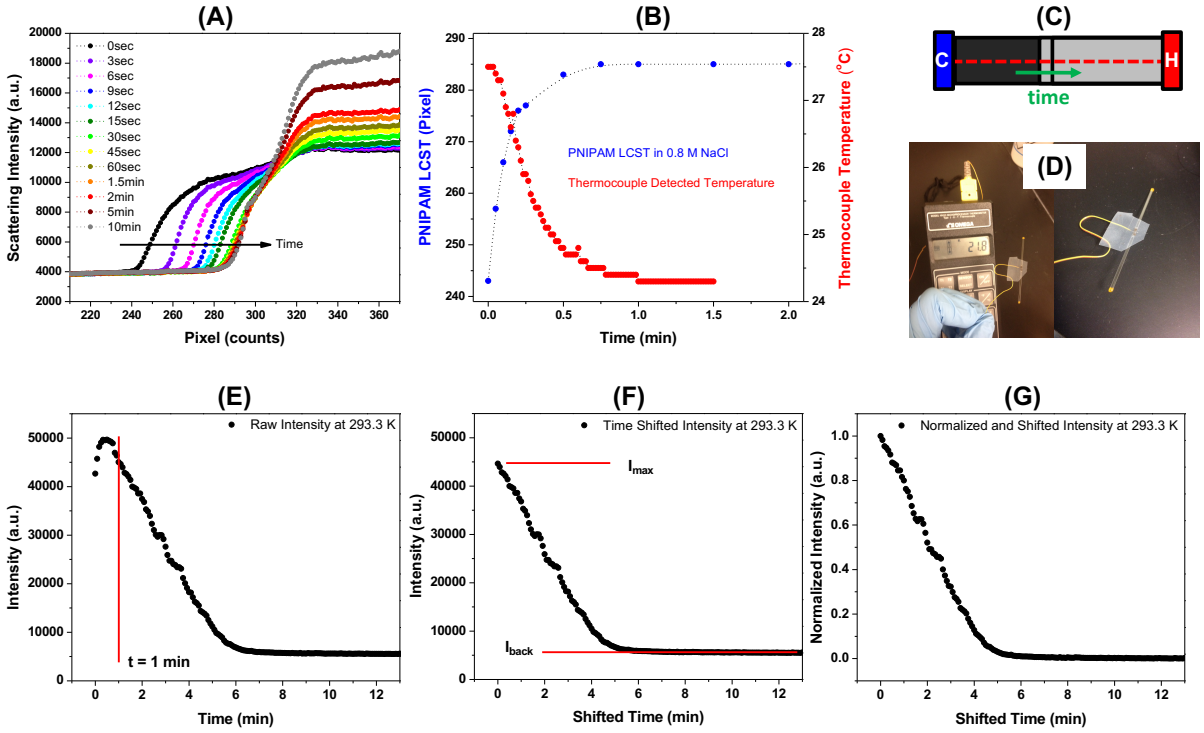

Figure S5. Control experiments on the establishment of a temperature gradient and a demonstration of the procedure for processing the light scattering kinetic data. (*A*) The line scans of a 10 mg/mL PNIPAM sample containing 0.8 M NaCl over time along a linear temperature gradient (278 – 318 K). The apparent LCST values (blue data points) determined from (*A*) are plotted in (*B*) along with a direct measurement of the temperature by a thermocouple (red data points) as a function of time. The shift of the LCST with time is illustrated schematically in (*C*). Pictures are provided to demonstrate the thermocouple measurement technique (*D*). (*E*-*G*) The sequential processing of raw data is shown for an isotherm at 293.3 K of a 90 mg/mL mAb and 20 mg/mL PEG-3350 solution. The light scattering intensity is plotted as a function of time in (*E*). Note, the vertical red line denotes the time required to reach a steady-state temperature gradient. After discarding the first minute of raw data, the intensity was plotted as a function of shifted time in (*F*). The normalized data are provided in (*G*).

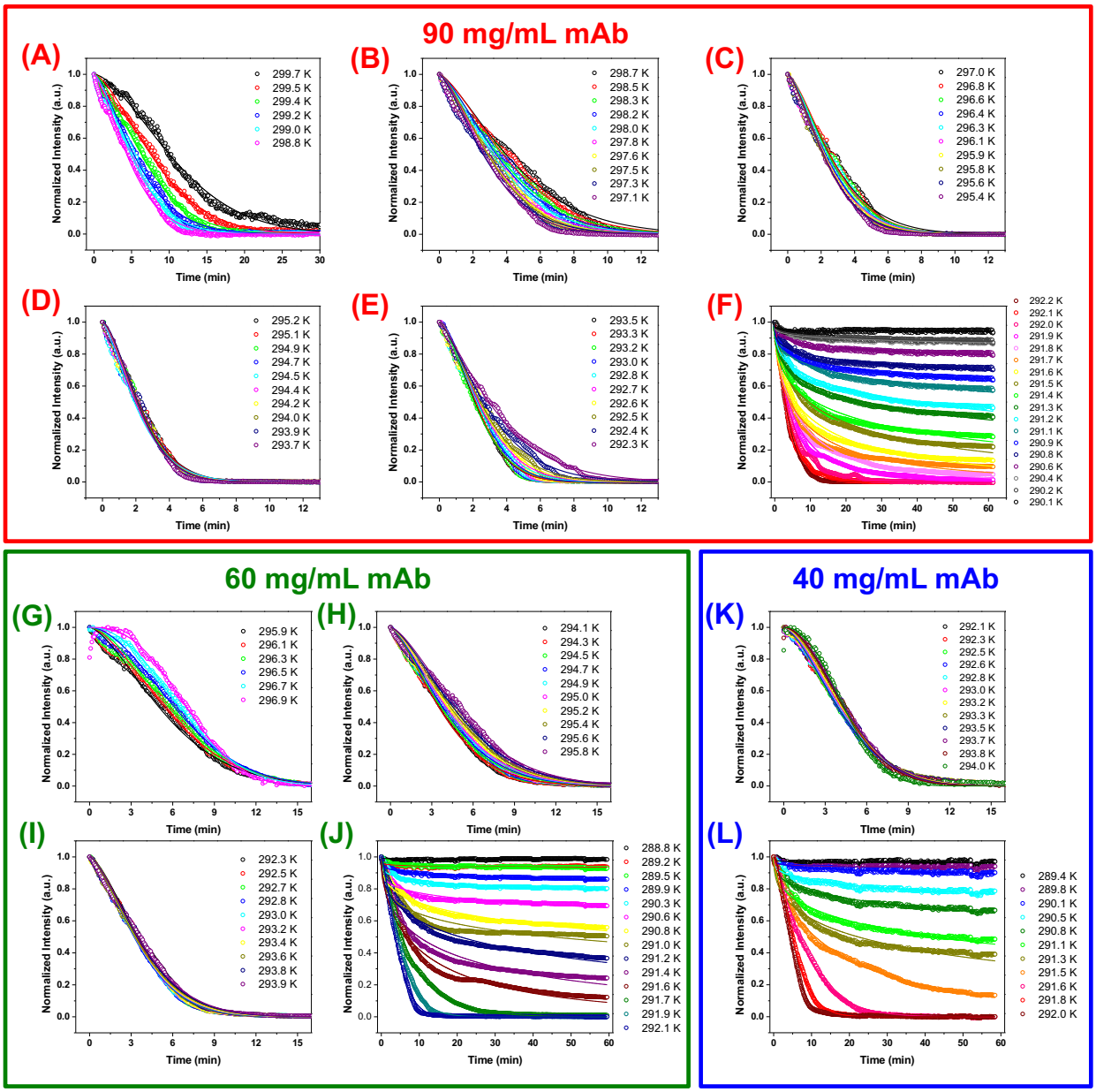

Figure S6. Normalized light scattering isotherms and KWW fits. The data are grouped into 3 panels corresponding to (red box) 90 mg/mL, (green box) 60 mg/mL, and (blue box) 40 mg/mL mAb concentrations all at 20 mg/mL PEG-3350. The 90 mg/mL data are displayed in 6 plots with decreasing temperature: (*A*) 299.7 – 298.8 K, (*B*) 298.7 – 297.1 K, (*C*) 297.0 – 295.4 K, (*D*) 295.2 – 293.7 K, (*E*) 293.5 – 292.3 K, and (*F*) 292.2 – 290.1 K. The 60 mg/mL data are displayed in 4 plots with decreasing temperature: (*G*) 296.8 – 295.8 K, (*H*) 295.7 – 294.0 K, (*I*) 293.8 – 292.2 K, and (*J*) 292.0 – 288.7 K. The 40 mg/mL data are displayed in 2 plots with decreasing temperature: (*K*) 294.0 – 292.1 K and (*L*) 292.0 – 289.4 K.

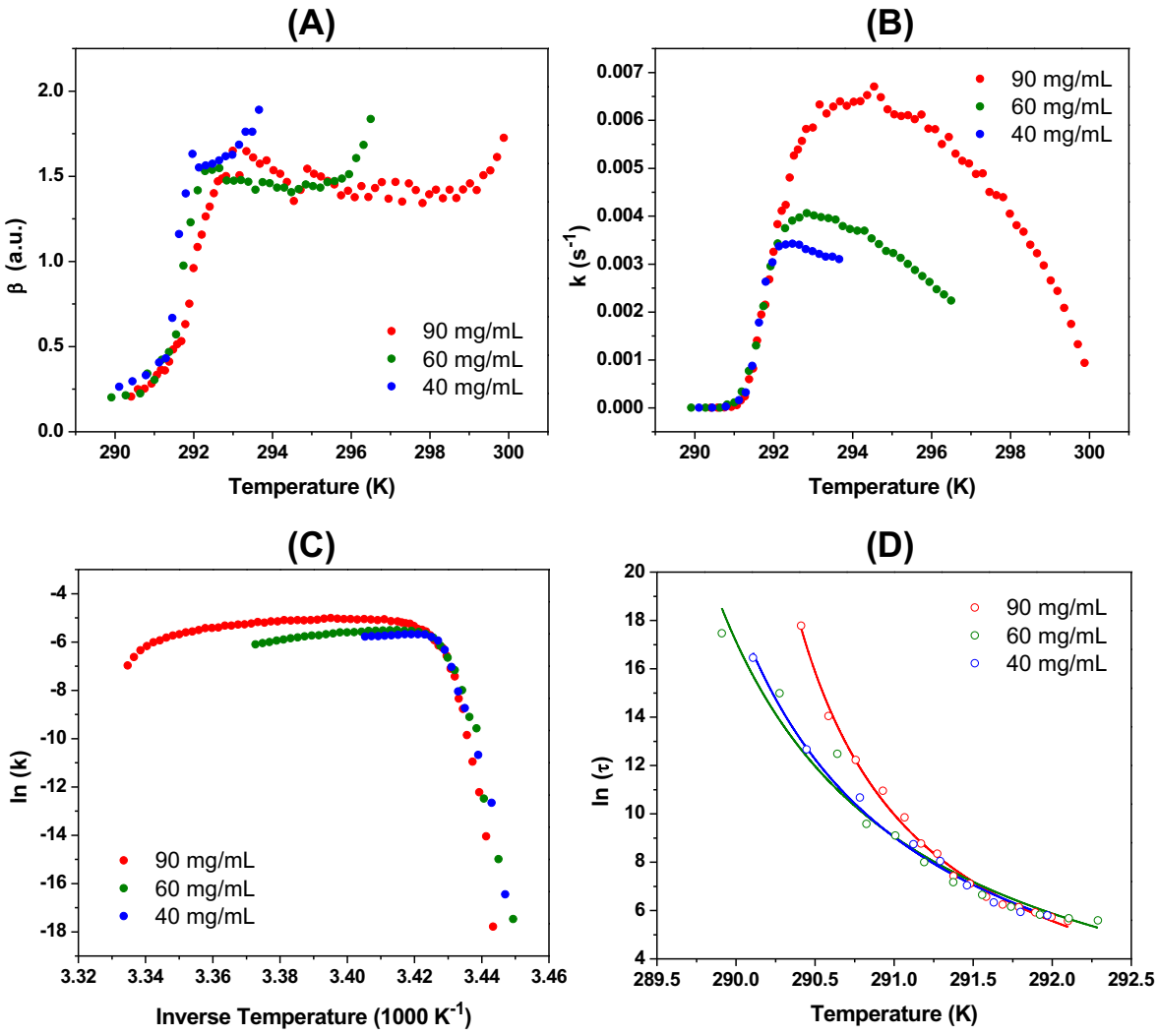

Figure S7. Summary of (*A*) the KWW cooperativity exponents and (*B*) the rate constants as a function of temperature for 3 mAb concentrations in 20 mg/mL PEG-3350. (*C*) An Arrhenius plot of ln(*k*) versus 1000/*T* and (D) a VFT plot of ln(*τ*) vs. *T* were prepared from the KWW parameters. The data points in (*A*-*D*) are colored according to the mAb concentration of either 40 mg/mL (blue), 60 mg/mL (green), or 90 mg/mL (red). The solid lines in (*D*) represent fits to the VFT model.

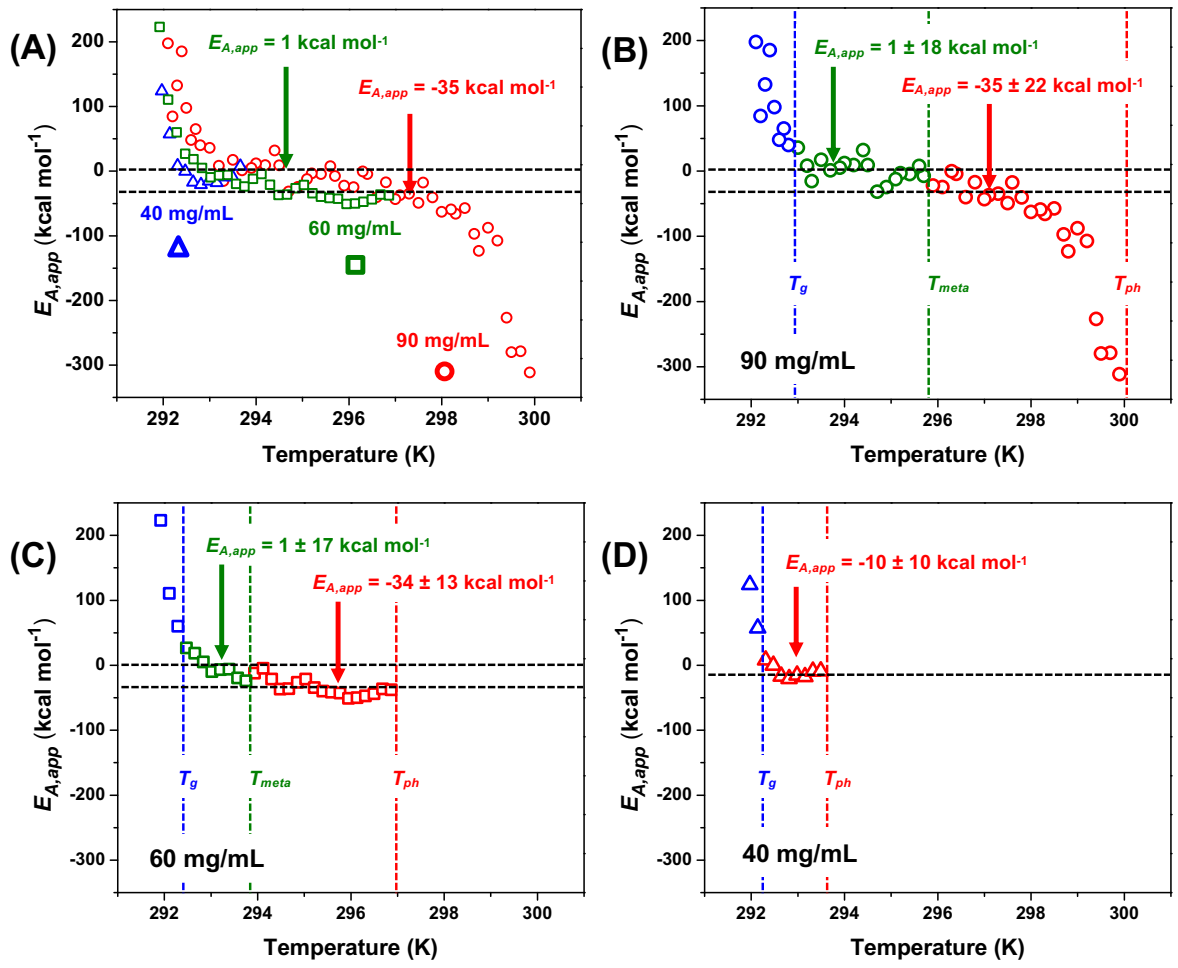

Figure S8. Apparent activation energies for ATPS formation, $E_{A,app}$, obtained from the Arrhenius plot in Fig. S7*C*. The values of $E_{A,app}$ are plotted a function of temperature for 90 (red circles), 60 (green squares), and 40 mg/mL mAb concentration (blue triangles) in (*A*). The 2 dashed horizontal black lines in (*A*) are guides to the eye and represent average values of $E_{A,app}$ determined in the spinodal (1 kcal mol^{-1}) and metastable (-35 kcal mol^{-1}) regions of the 90 and 60 mg/mL mAb samples. The $E_{A,app}$ values for the (*B*) 90, (*C*) 60, and (*D*) 40 mg/mL mAb concentrations are plotted separately for clarity. In (*B-D*), the data are divided into the metastable (red data), spinodal (green data), and gel (blue data) regions, which are demarcated by dashed vertical colored lines at T_{ph} (red lines), T_{meta} (green lines), and T_{gel} (blue lines). The dashed horizontal black lines in (*B-D*) represent the average values of $E_{A,app}$ determined for the spinodal (green text) and metastable (red text) regions. For the 90 mg/mL mAb sample in (*B*), the $E_{A,app}$ for the metastable region was determined only from the data between 295.9 - 298.3 K.

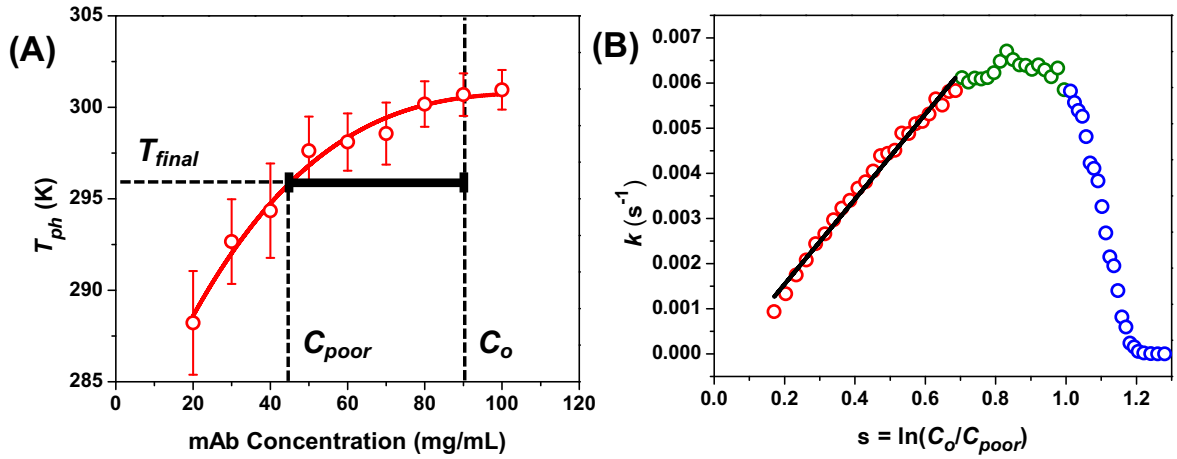

Figure S9. The relationship between supersaturation and the kinetics of ATPS formation. (*A*) Binodal curve of the colloidal phase diagram. The initial protein concentration, C_o, and equilibrium concentration of the protein-poor phase, C_{poor}, used to calculate supersaturation at a final temperature, T_{final}, are illustrated by the dashed vertical lines. (*B*) The rate constant of ATPS formation versus the supersaturation for the 90 mg/mL mAb sample. The data in (*B*) are colored in red, green, or blue to distinguish the metastable, spinodal, and gel regions, respectively.

Tables

Table S1. The fitted parameters of the VFT model for various mAb concentrations.

mAb Conc. (mg/mL)	τ_o (s)	T_o (K)	D (a.u.)
90	0.57	289.6	0.05
60	0.24	288.7	0.08
40	0.28	288.9	0.07

Movie Caption

Movie S1. Time-lapse video showing LLPS and ATPS formation of mAb solutions on the temperature gradient device. The video displays the data for 80, 90, and 100 mg/mL mAb solutions each containing 20 mg/mL PEG-3350, 15.5 mM NaCl, and 22.7 mM phosphate buffer at solution pH of 6.8. The mAb-containing capillaries are labeled with their concentration on the left-hand side of the video. Additional capillaries, containing 10 mg/mL PNIPAM, are included for calibration of the temperature gradient. The PNIPAM solution in the top-most capillary contains 1.5 M NaCl (LCST = 13.2 ºC), while the bottom-most capillary contains 0.1 M NaCl (LCST = 28.9 ºC). The video provides data for a total time of 20 minutes and 40 seconds, where the dark field images were acquired every 5 seconds. A time stamp is provided at the bottom-left corner of the video.

References

1. Mao H, Yang T, Cremer PS (2002) A microfluidic device with a linear temperature gradient for parallel and combinatorial measurements. *J Am Chem Soc* 124(16):4432–4435.

2. Annunziata O, et al. (2002) Effect of polyethylene glycol on the liquid–liquid phase transition in aqueous protein solutions. *Proc Natl Acad Sci* 99(22):14165–14170.

3. Wang Y, et al. (2013) Phase transitions in human IgG solutions. *J Chem Phys* 139(12):121904.

4. Liu C, et al. (1996) Phase separation in aqueous solutions of lens γ-crystallins: special role of γS. *Proc Natl Acad Sci U S A* 93(1):377–382.

5. Wang Y, Lomakin A, McManus JJ, Ogun O, Benedek GB (2010) Phase behavior of mixtures of human lens proteins Gamma D and Beta B1. *Proc Natl Acad Sci* 107(30):13282–13287.

6. Florence AT, Rogers JA (1971) Emulsion stabilization by non-ionic surfactants: experiment and theory. *J Pharm Pharmacol* 23(4):233–251.

7. Buscall R (1978) The properties of O/W emulsions stabilised with a non-ionic surfactant and surfactant-polymer mixtures. *Emulsions*, Progress in Colloid and Polymer Science., ed Weiss A (Steinkopff), pp 15–26.

8. Talapin DV, Rogach AL, Haase M, Weller H (2001) Evolution of an Ensemble of Nanoparticles in a Colloidal Solution: Theoretical Study. *J Phys Chem B* 105(49):12278–12285.

9. Kabalnov AS, Shchukin ED (1992) Ostwald ripening theory: applications to fluorocarbon emulsion stability. *Adv Colloid Interface Sci* 38:69–97.

10. Taylor P (1998) Ostwald ripening in emulsions. *Adv Colloid Interface Sci* 75(2):107–163.

11. Fortelný I, Živný A, JŮza J (1999) Coarsening of the phase structure in immiscible polymer blends. Coalescence or ostwald ripening? *J Polym Sci Part B Polym Phys* 37(3):181–187.

12. Buscall R, Davis SS, Potts DC (1979) The effect of long-chain alkanes on the stability of oil-in-water emulsions. The significance of ostwald ripening. *Colloid Polym Sci* 257(6):636–644.

13. Pan W, Vekilov PG, Lubchenko V (2010) Origin of anomalous mesoscopic phases in protein solutions. *J Phys Chem B* 114(22):7620–7630.

14. Li Y, Lubchenko V, Vorontsova MA, Filobelo L, Vekilov PG (2012) Ostwald-Like Ripening of the Anomalous Mesoscopic Clusters in Protein Solutions. *J Phys Chem B* 116(35):10657–10664.

15. Streets AM, Quake SR (2010) Ostwald Ripening of Clusters during Protein Crystallization. *Phys Rev Lett* 104(17):178102.

16. Shah M, Galkin O, Vekilov PG (2004) Smooth transition from metastability to instability in phase separating protein solutions. *J Chem Phys* 121(15):7505–7512.

17. Mattsson J, et al. (2009) Soft colloids make strong glasses. *Nature* 462(7269):83–86.

18. van der Scheer P, van de Laar T, van der Gucht J, Vlassopoulos D, Sprakel J (2017) Fragility and Strength in Nanoparticle Glasses. *ACS Nano* 11(7):6755–6763.

19. Mullin JW (2001) *Crystallization* (Butterworth-Heinemann, Oxford ; Boston). 4th ed.

20. Vekilov PG (2012) Phase diagrams and kinetics of phase transitions in protein solutions. *J Phys Condens Matter* 24(19):193101.

21. Berthoud A (1912) Théorie de la formation des faces d'un cristal. *J Chim Phys* 10:624–635.

22. Valeton J. J. P. (1924) I. Wachstum und Auflösung der Kristalle. III. *Z Für Krist - Cryst Mater* 60(1–6):1–38.

23. Petsev DN, Wu X, Galkin O, Vekilov PG (2003) Thermodynamic functions of concentrated protein solutions from phase equilibria. *J Phys Chem B* 107(16):3921–3926.

24. Heller P (1967) Experimental investigations of critical phenomena. *Rep Prog Phys* 30(2):731–826.

25. Broide ML, Berland CR, Pande J, Ogun OO, Benedek GB (1991) Binary-liquid phase separation of lens protein solutions. *Proc Natl Acad Sci U S A* 88(13):5660–5664.

26. Muschol M, Rosenberger F (1997) Liquid–liquid phase separation in supersaturated lysozyme solutions and associated precipitate formation/crystallization. *J Chem Phys* 107(6):1953–1962.

27. Atkins P, Paula J de (2009) The rates of chemical reactions. *Physical Chemistry* (W. H. Freeman, New York), pp 782–830. 9th edition.

28. Smoluchowski MV (1916) Drei Vortrage uber Diffusion, Brownsche Bewegung und Koagulation von Kolloidteilchen. *Z Phys* 17:557–585.

29. Tempel M van den (1953) Stability of oil-in-water emulsions II: Mechanism of the coagulation of an emulsion. *Recl Trav Chim Pays-Bas* 72(5):433–441.

30. Yefremova Y, et al. (2017) Apparent activation energies of protein-protein complex dissociation in the gas-phase determined by electrospray mass spectrometry. *Anal Bioanal Chem* 409(28):6549–6558.